DOT/FAA/AR-00/25

Office of Aviation Research
Washington, D.C. 20591

Experimental Investigations of Material Models for Ti-6Al-4V Titanium and 2024-T3 Aluminum

September 2000
Final Report

This document is available to the U.S. public through the National Technical Information Service (NTIS), Springfield, Virginia 22161.

U.S. Department of Transportation
Federal Aviation Administration

NOTICE

This document is disseminated under the sponsorship of the U.S. Department of Transportation in the interest of information exchange. The United States Government assumes no liability for the contents or use thereof. The United States Government does not endorse products or manufacturers. Trade or manufacturer's names appear herein solely because they are considered essential to the objective of this report. This document does not constitute FAA certification policy. Consult your local FAA aircraft certification office as to its use.

This report is available at the Federal Aviation Administration William J. Hughes Technical Center's Full-Text Technical Reports page: actlibrary.tc.faa.gov in Adobe Acrobat portable document format (PDF).

Technical Report Documentation Page

1. Report No.	2. Government Accession No.	3. Recipient's Catalog No.
DOT/FAA/AR-00/25		

4. Title and Subtitle	5. Report Date
EXPERIMENTAL INVESTIGATIONS OF MATERIAL MODELS FOR Ti-6Al-4V TITANIUM AND 2024-T3 ALUMINUM	September 2000
	6. Performing Organization Code
7. Author(s)	8. Performing Organization Report No.
Donald R. Lesuer	
9. Performing Organization Name and Address	10. Work Unit No. (TRAIS)
Lawrence Livermore National Laboratory Livermore, CA 94551	11. Contract or Grant No. DTFA03-97-Z-90007
12. Sponsoring Agency Name and Address	13. Type of Report and Period Covered
U.S. Department of Transportation Federal Aviation Administration Office of Aviation Research Washington, DC 20591	Final Report ANM-100 and ANE-100

15. Supplementary Notes

The Federal Aviation Administration William J. Hughes Technical Center COTR is William C. Emmerling

16. Abstract

The report describes studies of the deformation and failure behavior of Ti-6Al-4V titanium and 2024-T3 aluminum. This work was accomplished by the Lawrence Livermore National Laboratory under an Interagency Agreement between the Federal Aviation Administration (FAA) William J. Hughes Technical Center and the Department of Energy (DOE). The work was accomplished under the FAA's Aircraft Catastrophic Failure Prevention Program as part of its research into the turbine engine uncontainment event. Data was obtained at high strain rates and large strains using the split Hopkinson pressure bar method. This information, plus additional data from the literature, were used to critically evaluate the ability of the Johnson-Cook material model to represent the deformation and failure response of Ti-6Al-4V and 2024-T3 under conditions relevant to simulations of engine containment and the influence of uncontained engine debris on aircraft structures. This model is being used in the DYNA3D finite element code, which is being developed/validated for evaluating aircraft/engine designs relative to the federal airworthiness standards and for improving mitigation/containment technology. The results of this experimental work were used to define a new set of material constants for the strength component of the Johnson-Cook model for Ti-6Al-4V and 2024-T3.

17. Key Words	18. Distribution Statement
Turbine engine uncontainment, Johnson-Cook model, Material constants, DYNA3D	Document is available to the public through the National Technical Information Service (NTIS), Springfield, Virginia 22161.

19. Security Classif. (of this report)	20. Security Classif. (of this page)	21. No. of Pages	22. Price
Unclassified	Unclassified	41	

Form DOT F1700.7 (8-72) **Reproduction of completed page authorized**

ACKNOWLEDGMENTS

The authors are indebted to Mary LeBlanc for the split Hopkinson pressure bar testing and Robert Kershaw for metallography. The work was performed under the auspices of the U.S. Department of Energy by the Lawrence Livermore National Laboratory under contract No. W-7405-ENG-48.

TABLE OF CONTENTS

		Page
EXECUTIVE SUMMARY		ix
1.	INTRODUCTION	1
1.1	Background and Motivation	1
1.2	Johnson-Cook Material Model	2
2.	SPECIMEN CONFIGURATION AND EXPERIMENTAL PROCEDURES	3
2.1	Material and Test Specimens	3
2.2	Experimental Procedures	5
3.	TEST RESULTS	5
3.1	Data for Ti-6Al-4V Titanium	5
3.1.1	Stress-Strain Data for Ti-6A1-4V	5
3.1.2	Microstructural Characterization	7
3.1.3	Data Analysis	10
3.2	Data for 2024-T3 Aluminum	13
3.2.1	Stress-Strain Data for 2024-T3	13
3.2.2	Microstructural Characterization	14
3.2.3	Data Analysis	14
4.	ANALYSIS OF JOHNSON-COOK MATERIAL MODEL	16
5.	NEW CONSTANTS FOR JOHNSON-COOK MATERIAL MODEL	18
5.1	Ti-6Al-4V Titanium	18
5.2	2024-T3 Aluminum	22
6.	SUMMARY	25
7.	REFERENCES	26
APPENDIX A—Procedures for Obtaining Parameters for Johnson-Cook Material Model		

LIST OF FIGURES

Figure		Page
1	Microstructure of Ti-6Al-4V Alloy	3
2	Microstructure of 2024-T3 Alloy	4
3	Stress-Strain Response for Ti-6Al-4V Alloy Tested in Compression at a Strain Rate of 4500 s^{-1}	6
4	Stress-Strain Response for Ti-6Al-4V Alloy Tested in Tension at a Strain Rate of 5200 s^{-1}	7
5	Photograph of Ti-6Al-4V Sample After Testing in Compression	8
6	Fracture Surface of Ti-6Al-4V Sample Tested in Compression	8
7	Shear Band in Ti-6Al-4V Sample After Testing in Compression	8
8	Cross Section of Ti-6Al-4V Sample After Testing in Tension	9
9	Fracture Surface of Ti-6Al-4V Sample Tested in Tension	9
10	Comparison of the High-Strain Rate, Stress-Strain Response of the Ti-6Al-4V Alloy in Tension and Compression	10
11	Comparison of the Stress-Strain Rate Response of Ti-6Al-4V Alloy Obtained From This Study as Well as Other Studies From the Literature	12
12	Stress-Strain Response for 2024-T3 Alloy Tested in Compression at a Strain Rate of 4000 s^{-1}	13
13	Stress-Strain Response for 2024-T3 Alloy Tested in Tension at a Strain Rate of 8000 s^{-1}	14
14	Comparison of the High-Strain Rate, Stress-Strain Response of 2024-T3 Alloy in Tension and Compression	15
15	Stress-Strain Rate Data Obtained by Johnson for the Ti-6Al-4V Alloy at a Plastic Strain of 0.002	17
16	Comparison of the High-Strain Rate, Stress-Strain Response of the Ti-6Al-4V Alloy Predicted by the Johnson-Cook Material Model (Using the New Material Parameters) With Experimental Data in Tension and Compression	19

17 Comparison of the Low-Strain Rate (0.0001 s^{-1}), Stress-Strain Response of the Ti-6Al-4V Alloy as Predicted by the Johnson-Cook Material Model (Using the New Material Parameters) With Experimental Data in Tension 19

18 Comparison of the Stress-Strain Rate Response of the Ti-6Al-4V Alloy as Predicted by the Johnson-Cook Material Model (Using the New Material Parameters) With Experimental Data. Calculations and Data Were Taken at a Strain of 0.04. 20

19 Comparison of the Stress-Temperature Response of the Ti-6Al-4V Alloy as Predicted by the Johnson-Cook Material Model (Using the New Material Parameters) With Experimental Data 20

20 Predicted Adiabatic Stress-Strain Response for the Ti-6Al-4V Alloy in Tension, Shear, and Compression at a Strain Rate of 5000 s^{-1} 22

21 Comparison of the High-Strain Rate, Stress-Strain Response of the 2024-T3 Alloy Predicted by the Johnson-Cook Material Model (Using the New Material Parameters) With Experimental Data in Tension and Compression 23

22 Comparison of the Low-Strain Rate (0.0005 s^{-1}), Stress-Strain Response of the 2024-T3 Alloy as Predicted by the Johnson-Cook Material Model (Using the New Material Parameters) With Experimental Data in Tension 23

23 Comparison of the Stress-Strain Rate Response of the 2024-T3 Alloy as Predicted by the Johnson-Cook Material Model (Using the New Material Parameters) With Experimental Data 24

24 Comparison of the Stress-Temperature Response of the 2024-T3 Alloy as Predicted by the Johnson-Cook Material Model (Using the New Material Parameters) With Experimental Data 24

25 Predicted Adiabatic Stress-Strain Response for the 2024-T3 Alloy in Tension, Shear, and Compression at a Strain Rate of 6000 s^{-1} 25

LIST OF TABLES

Table		Page
1	Chemical Composition of 2024-T3	4
2	Manufacturer Supplied Static Properties for 2024-T3	4
3	True Strain at Fracture for Ti-6Al-4V and 2024-T3	6
4	High-Rate Literature Data for Annealed Ti-6Al-4V	11
5	Instability Strains for 2024-T351 in Compression	16
6	Original Parameters for Johnson-Cook Material Model	17
7	Physical Properties of Ti-6Al-4V and 2024-T3	18
8	New Parameters for Johnson-Cook Material Model	18

EXECUTIVE SUMMARY

This report describes studies of the deformation and failure behavior of Ti-6Al-4V titanium and 2024-T3 aluminum. Data were obtained at high strain rates and large strains using the split Hopkinson pressure bar technique. This and additional data from the literature, were used to critically evaluate the ability of the Johnson-Cook material model to represent the deformation and failure response of Ti-6Al-4V and 2024-T3 under conditions relevant to simulations of engine containment and the influence of uncontained engine debris on aircraft structures. This model is being used in the DYNA3D finite element code, which is being developed/validated for evaluating aircraft/engine designs relative to the federal airworthiness standards and for improving mitigation/containment technology. The results of the experimental work reported here were used to define a new set of material constants for the strength component of the Johnson-Cook model for Ti-6Al-4V and 2024-T3. The capabilities and limitations of the model are reviewed. The model can accurately represent the stress-strain response of the materials. The major concern with the Johnson-Cook material model is its ability to accurately represent the stress-strain rate response at strain rates greater than 10^3 - 10^4 s^{-1}. Additional work is also needed to adequately account for failure via shear localization, which was the dominant failure mode at high strain rates in both materials. Failure modeling in both Ti-6Al-4V and 2024-T3 will be considered further in future reports.

1. INTRODUCTION.

1.1 BACKGROUND AND MOTIVATION.

The Program Plan for the Federal Aviation Administration (FAA) Aircraft Catastrophic Failure Prevention Program has established a framework for research and development that will produce standard tools for evaluating aircraft and engine designs relative to the Federal airworthiness standards and for improving mitigation and containment technology. A key tool being developed and validated under this program is a finite element code DYNA3D capable of accurate simulations involving engine containment and the influence of uncontained engine debris on aircraft structures. DYNA3D [1] is a nonlinear, explicit, three dimensional finite element code that was developed at the Lawrence Livermore National Laboratory (LLNL) to study a wide range of solid mechanics problems including impact and perforation problems. A critical component of the code is a validated material model(s) that can adequately represent the penetration and perforation of aircraft and engine materials. Material models, which can adequately represent the deformation response during high-rate loading, typical of such an event, must account for large strains (and the resulting strain hardening or softening) as well as large changes in strain rate and temperature. Several models have been developed which can represent, with varying degrees of accuracy, the high rate deformation response of materials. Examples include models by Johnson-Cook (JC) [2-4], Zerilli-Armstrong [5-7], Steinberg-Guinan [8] and Follansbee-Kocks (mechanical threshold stress model) [9]. Of these models, the JC model is the most widely used and has been introduced into the DYNA3D code. The JC model was developed during the 1980s to study impact, ballistic penetration, and explosive detonation problems. The model has proven to be very popular and has been used extensively in national laboratories, military laboratories, and private industry to study high-rate, large strain problems. In addition, the participants in this program (including Allied Signal Engines, Boeing Commercial Aircraft Corporation, Lawrence Livermore National Laboratory and United Technologies, (Pratt & Whitney) are using the JC model and the DYNA3D code for simulations of containment and the mitigation of uncontained engine debris. The JC material model has both a strength [2,3,10] and a damage component [4]. The damage component has a cumulative damage law which can be used to assess failure.

This report describes studies of the deformation and failure behavior of Ti-6Al-4V titanium and 2024-T3 aluminum. Data were obtained at high strain rates and large strains using state-of-the-art mechanical testing techniques (the split Hopkinson pressure bar technique described in section 2.2). These data and additional data from the literature, were used to critically evaluate the ability of the JC model to represent the deformation and failure response of these materials under conditions relevant to simulations of engine containment and the influence of uncontained engine debris on aircraft structures. The results were used to define a new set of material constants for the strength component of the JC model for Ti-6Al-4V and 2024-T3. The failure modeling of these materials will be revisited in a future report.

1.2 JOHNSON-COOK MATERIAL MODEL.

The formulation for the JC model is empirically based. The JC model represents the flow stress with an equation of the form

$$\sigma = [A + B\varepsilon^n][1 + C\ln\dot{\varepsilon}^*][1 - T^{*m}] \tag{1}$$

where σ is the effective stress, ε is the effective plastic strain, $\dot{\varepsilon}^*$ is the normalized effective plastic strain rate (typically normalized to a strain rate of 1.0 s^{-1}), n is the work hardening exponent and A, B, C, and m are constants. The quantity T* is defined as

$$T^* = (T-298)/(T_{melt}-298) \tag{2}$$

where T_{melt} is the melting temperature and is typically taken as the solidus temperature for an alloy. The strength of the material is thus a function of strain, strain rate, and temperature. The model assumes that the strength is isotropic and independent of mean stress.

The values of A, B, C, n, and m are determined from an empirical fit of flow stress data (as a function of strain, strain rate, and temperature) to equation 1. For high rate deformation problems, we can assume that an arbitrary percentage of the plastic work done during deformation produces heat in the deforming material. For many materials, 90-100 percent of the plastic work is dissipated as heat in the material. Thus, the temperature used in equation 1 can be derived from the increase in temperature according to the following expression

$$\Delta T = \frac{\alpha}{\rho c}\int \sigma(\varepsilon)\, d\varepsilon \tag{3}$$

where ΔT is the temperature increase, α is the percentage of plastic work transformed to heat, c is the heat capacity and ρ is the density.

Fracture in the JC material model is derived from the following cumulative damage law

$$D = \Sigma \frac{\Delta\varepsilon}{\varepsilon_f} \tag{4}$$

in which

$$\varepsilon_f = [D_1 + D_2\exp(D_3\sigma^*)][1+D_4\ln\dot{\varepsilon}^*][1+D_5T^*] \tag{5}$$

where $\Delta\varepsilon$ is the increment of effective plastic strain during an increment in loading and σ^* is the mean stress normalized by the effective stress. The parameters D_1, D_2, D_3, D_4, and D_5 are constants. Failure is assumed to occur when D = 1. The current failure strain in the problem (ε_f), and thus the accumulation of damage, is a function of mean stress, strain rate, and temperature.

2. SPECIMEN CONFIGURATION AND EXPERIMENTAL PROCEDURES.

2.1 MATERIAL AND TEST SPECIMENS.

The Ti-6Al-4V alloy evaluated in this study was purchased from RMI Titanium Company of Niles, Ohio in the form of a hot-rolled and annealed plate. The annealing heat treatment was done at 790°C for 1 hour followed by furnace cooling. Before testing, samples were annealed at 730°C for 1 hour and air cooled. The alloy was processed to conform to specification AMS 4911, which is typically used for Ti-6Al-4V for aircraft containment structures. For the Ti-6Al-4V tests, the compression sample diameter was 5 mm and for the 2024-T3 tests the compression sample diameter was 4 mm. The tension samples were flat (1 mm thick) with a gage length of 5 mm and gage width of 2.5 mm. This specification was also used for procurement of Ti-6Al-4V plate for ballistic testing (also being conducted in this program) including sub-scale tests by LLNL (12.7-mm-thick plate) and full-scale tests by Pratt and Whitney (19.1-mm-thick plate). The microstructure of the as-tested material is shown in figure 1 and the orientations of the 0°, 90°, and normal (n, through thickness) directions are indicated in the figure. The microstructure consists of roughly equiaxed alpha and transformed beta phase, which is a typical microstructure for the Ti-6Al-4V alloy manufactured to the AMS 4911 specification. Compression Hopkinson bar samples were machined with the compression axis parallel to the three orthogonal directions shown in figure 1. Tensile Hopkinson bar samples were prepared with the tensile axis parallel to the two in-plane directions (0° and 90°) shown in figure 1.

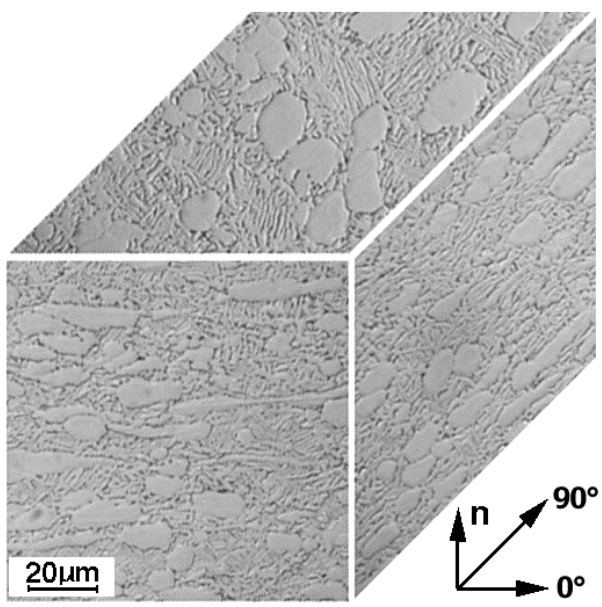

FIGURE 1. MICROSTRUCTURE OF Ti-6Al-4V ALLOY

The 2024-T3 alloy evaluated in this study was purchased from the Kaiser Aluminum, Trentwood, WA Plant in the form of a 4-mm-thick plate. The material was manufactured to specifications AMS 4037 (revision M) and ASTM-B-209 (revision 96). The chemical composition and mechanical properties of the tested alloy, as supplied by Kaiser, are provided in tables 1 and 2,

respectively. The chemical composition and mechanical properties conform to the requirements of the specifications. The microstructure of the as-tested material is shown in figure 2 and the orientations of the 0° (rolling direction), 90°, and normal (n, through thickness) directions are indicated in the figure. The microstructure consists of highly flattened grains with an aspect ratio of about 3 to 1 in the plane of the sheet. Compression Hopkinson bar samples were machined with the compression axis parallel to the three orthogonal directions shown in figure 2. Tensile Hopkinson bar samples were prepared with the tensile axis parallel to the two in-plane directions (0° and 90°) shown in figure 2.

TABLE 1. CHEMICAL COMPOSITION OF 2024-T3

Aluminum	Balance
Copper	4.76%
Magnesium	1.38%
Manganese	0.65%
Iron	0.22%
Silicon	0.08%
Zinc	0.07
Titanium	0.03
Chromium	0.01

TABLE 2. MANUFACTURER SUPPLIED STATIC PROPERTIES FOR 2024-T3

Yield Strength (MPa)		Ultimate Tensile Strength (MPa)		Elongation (%)	
minimum	maximum	minimum	maximum	minimum	maximum
327	330	474	477	16.0	18.2

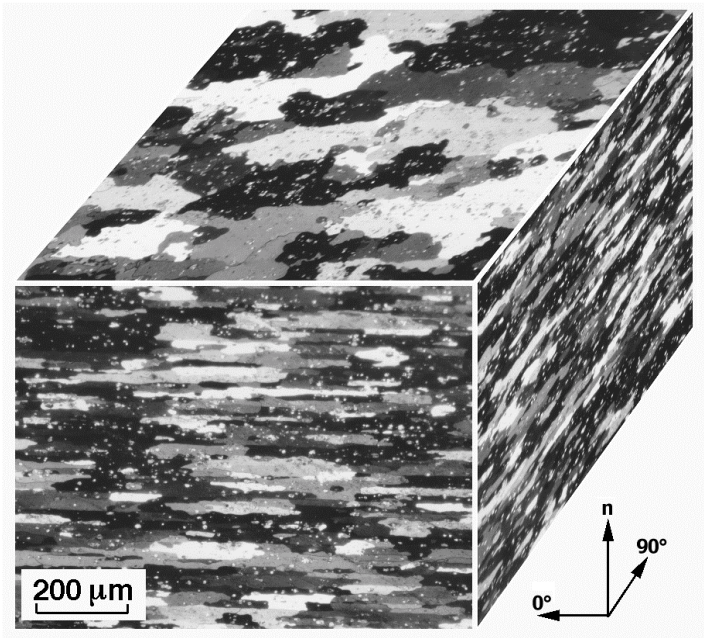

FIGURE 2. MICROSTRUCTURE OF 2024-T3 ALLOY

2.2 EXPERIMENTAL PROCEDURES.

High-rate testing was done in both compression and tension using the split Hopkinson pressure bar technique [11] and data was obtained at strain rates of 10^3 - 10^4 s^{-1}. In the split Hopkinson pressure bar technique, a specimen of the Ti-6Al-4V alloy or the 2024-T3 alloy is placed between two long bars made of Ti-6Al-4V. A striker bar is propelled toward one of the pressure bars (the input bar). Upon impact, an elastic stress wave is introduced into the input bar. This stress wave travels down the bar and, at the specimen-bar interface, a portion of this wave is transferred into the sample, which causes the sample to deform. Depending on the details of the experimental setup, the sample can be loaded in either tension or compression. For additional information, see references 11 and 12. The compression samples were right circular cylinders with the diameter equal to the height. The compression surfaces were polished flat prior to testing and no lubrication was used.

In the compression tests, the strain histories for the incident and transmitted waves in the elastic pressure bars were measured and analyzed to determine the nominal stress-strain and strain-rate response of the samples. In the tension tests, the strain histories in the elastic pressure bars were used to obtain the stress-time response of the sample. A high-speed framing camera was used to follow the deformation behavior of the tension samples. The photographic images from this camera were used to obtain the strain and strain rate response of the sample. The photographic images were also studied carefully to determine the strain at which fracture occurred.

3. TEST RESULTS.

3.1 DATA FOR Ti-6Al-4V TITANIUM.

3.1.1 Stress-Strain Data for Ti-6Al-4V.

3.1.1.1 Compression Data for Ti-6Al-4V.

The true stress-true strain response for the Ti-6Al-4V alloy in compression is shown in figure 3. The nominal strain rate in these tests was 4500 s^{-1}. Two tests are shown for each of the three testing orientations evaluated. (Stress and strain in compression are negative; however, for the ease of comparison with other data, all stress and strain data reported here are plotted using their absolute values). The repeatability of the test data is excellent. Samples tested in the normal and in-plane 0° orientations produced stress-strain curves that are virtually identical. Samples tested in the 90° orientation produced stress-strain curves that are about 250 MPa higher than the curves in the other two orientations. Due to the texture present in the hot-rolled plate, Conrad et al. [13] showed that hot-rolled Ti can develop a texture when a crystallographic direction is nearly parallel to the rolling direction. Such textures in hot-rolled Ti-6Al-4V are well known for promoting anisotropic flow behavior at quasi-static strain rates. Data show that for Ti-6Al-4V, the tensile properties can vary by 200 MPa with direction in the sheet [14]. The oscillations in the stress-strain curve result from the fact that data is gathered from an input bar, which has an oscillating stress-time history. This oscillating stress-time history results from complex wave propagation effects associated with the propagation of a stress pulse of finite width down a long/thin input bar. The stress-time history in the sample is considerably smoother, since the

sample is short (relative to the input bar and the striker) and wave reflections remove much of the oscillation. For detailed discussion and analysis, see references 15 and 16. The stress-strain response of the sample is considerably more uniform and can be taken as the average curve through the data in figure 3. The fracture strains for the Ti-6Al-4V alloy tested in compression are shown in table 3. Fracture in the samples was assumed to occur at the point of pronounced softening, i.e., the point in figure 3 where the curves drop off.

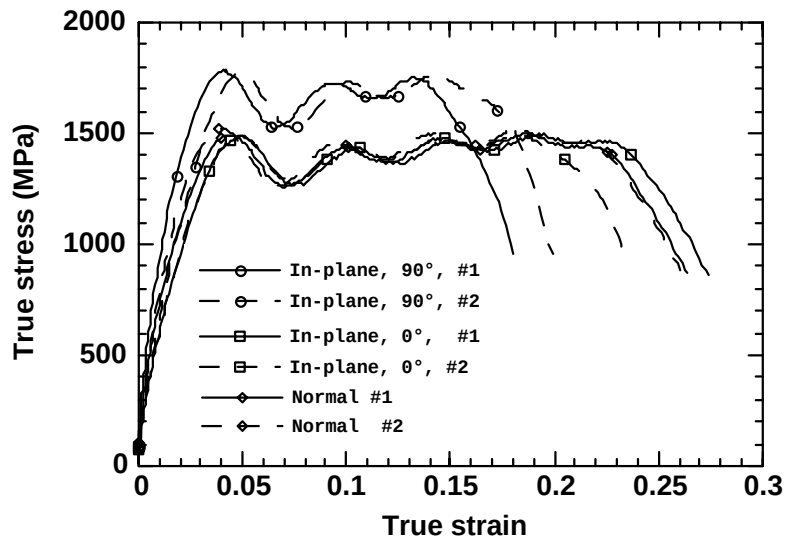

FIGURE 3. STRESS-STRAIN RESPONSE FOR Ti-6Al-4V ALLOY TESTED INCOMPRESSION AT A STRAIN RATE OF 4500 s^{-1}

TABLE 3. TRUE STRAIN AT FRACTURE FOR Ti-6Al-4V AND 2024-T3

	Ti-6Al-4V		2024-T3	
	Strain Rate (s^{-1})	Fracture Strain	Strain Rate (s^{-1})	Fracture Strain
0° Compression #1	4500	0.19	4000	>0.54
0° Compression #2	4500	0.23	4000	>0.72
90° Compression #1	4500	0.14	4000	>0.54
90° Compression #2	4500	0.18	4000	>0.64
Normal Compression #1	4500	0.23	4000	>0.54
Normal Compression #2	4500	0.22	4000	>0.54
0° Tension	5200	0.22	8000	0.29
90° Tension	5200	0.22	8000	0.28

3.1.1.2 Tension Data for Ti-6Al-4V.

The true stress-true strain response for the Ti-6Al-4V alloy in tension is shown in figure 4. The nominal strain rate in these tests was 5200 s^{-1}. Two tests were conducted and test results are shown for both in-plane orientations. In contrast to the data in compression, the data in tension shows that the stress-strain response in the plane is the same in all directions (isotropic) despite the obvious texture present in the plate as revealed by the anisotropic results in compression.

Analysis of figures 3 and 4 shows that, with the exception of the compression tests in the 90° orientation, the stress-strain response is isotropic and independent of testing orientation (tension vs. compression). This point will be discussed further in section 3.1.3. Data for elastic loading of the sample (in both tension and compression) cannot be obtained in these tests due to wave propagation effects. The stress-strain curves shown in figures 3 and 4 can be considered valid once the samples have yielded plastically. Once significant plastic strains are developed, stress and strain rate uniformity are achieved in the sample. As mentioned in section 2.2, the photographic images obtained from the framing camera were used to establish the strain and location in the tensile samples at which fracture initiated; these true strains at fracture are indicated in table 3. Fracture of the tensile samples was first observed at the edges of the samples. For both Ti-6Al-4V tensile samples tested, fracture initiated at maximum stress as shown on the stress-strain curves in figure 4.

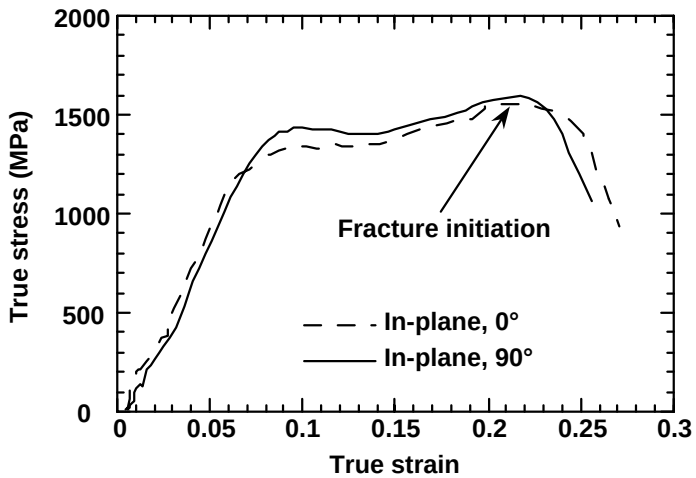

FIGURE 4. STRESS-STRAIN RESPONSE FOR Ti-6Al-4V ALLOY TESTED IN TENSION AT A STRAIN RATE OF 5200 s^{-1}

3.1.2 Microstructural Characterization.

Both the tension and compression samples were characterized after fracture using optical metallography and scanning electron microscopy. A typical compression sample after testing is shown in figure 5. This sample, which was tested with the compression axis parallel to the normal direction in the plate, failed along a shear plane that is oriented at 45° to the axis of loading. All compression samples of the Ti-6Al-4V alloy, irrespective of orientation, failed along a shear plane similar to figure 5. The sample shows very uniform deformation with no indications of barreling. The fracture surface of this sample, which is shown in figure 6, exhibits very shallow voids that are approximately 5 µm in diameter and experienced growth and interlinkage due to shear deformation. Figure 7 shows a typical adiabatic shear band observed in the compression samples. The width of the shear band is approximately 15 µm. All compression samples tested, irrespective of orientation, failed due to adiabatic shear localization.

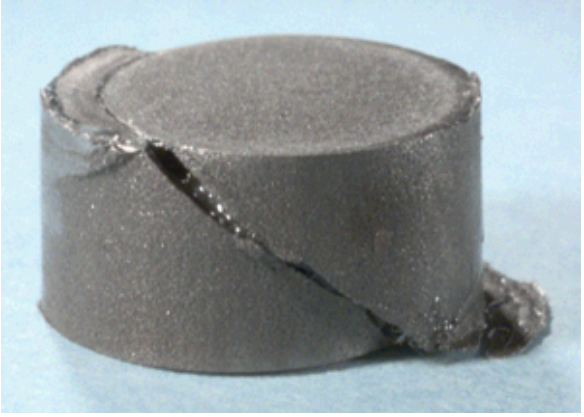

FIGURE 5. PHOTOGRAPH OF Ti-6Al-4V SAMPLE AFTER TESTING IN COMPRESSION

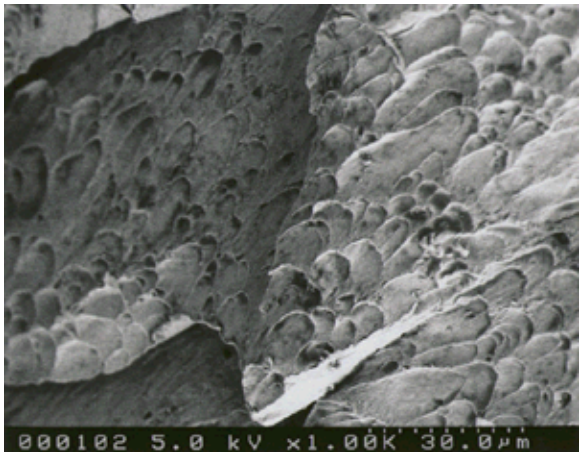

FIGURE 6. FRACTURE SURFACE OF Ti-6Al-4V SAMPLE TESTED IN COMPRESSION

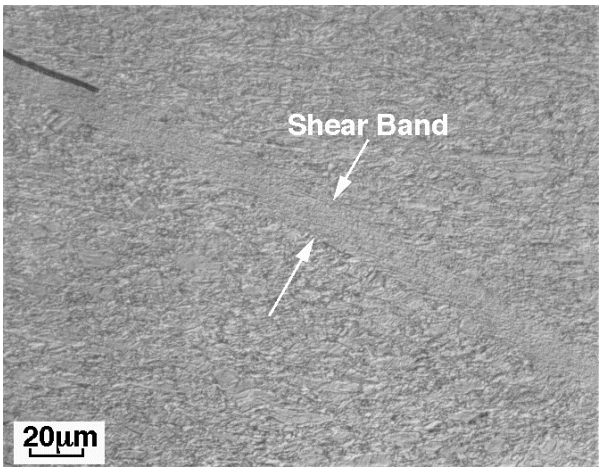

FIGURE 7. SHEAR BAND IN Ti-6Al-4V SAMPLE AFTER TESTING IN COMPRESSION

The cross-section of a fractured tensile sample (tensile axis was parallel to the 0° direction) is shown in figure 8. The normal and 0° directions are indicated. The sample failed in shear with the shear fracture propagating through the thickness of the plate. Figure 9 shows the fracture surface of the tensile sample tested with the tensile axis parallel to the 90° direction. As with the compression sample, shallow voids are observed (about 5 µm in diameter) that grew due to shear deformation. These fracture characteristics are representative of all tensile failures observed in the Ti-6Al-4V alloy. It was concluded that the specimen fracture in both tension and compression resulted from adiabatic shear localization. The failure modes in the Hopkinson bar samples were compared with the results of post-failure analysis conducted by Pratt & Whitney on a Ti-6Al-4V fan case (which was impacted by a fan blade) [17]. Both the Hopkinson bar samples reported here and the fan case study showed failures involving shear localization. In both cases, the width of the shear bands was observed to be approximately 15 µm.

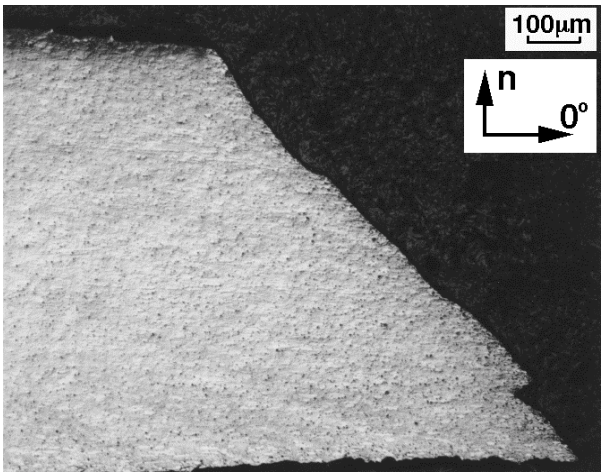

FIGURE 8. CROSS SECTION OF Ti-6Al-4V SAMPLE AFTER TESTING IN TENSION

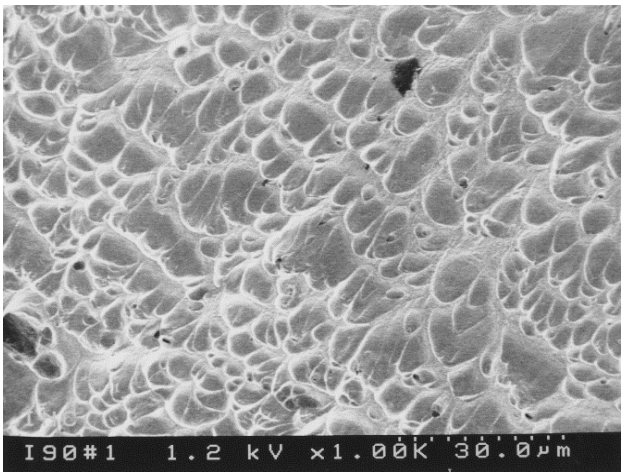

FIGURE 9. FRACTURE SURFACE OF Ti-6Al-4V SAMPLE TESTED IN TENSION

3.1.3 Data Analysis.

The stress-strain response in tension and compression are compared in figure 10 for Ti-6Al-4V samples tested in the 0° orientation. The results show that, in the region of valid data (large-scale plastic flow), the two curves coincide (indicated as "LLNL-compression" and "LLNL-tension"). Thus, for loading in the 0° direction, the stress-strain behavior of the hot-rolled Ti-6Al-4V alloy is insensitive to the sign of the applied stress (tension versus compression). In section 3.1, it was noted that the flow behavior was isotropic in tension but anisotropic in compression. Analysis of figures 3, 4, and 6 shows that, with the exception of the 90° orientation in compression, a common σ - ε curve results. Thus, with the exception of this 90° orientation, the stress-strain behavior of the Ti-6Al-4V alloy is isotropic and insensitive to mean stress, which is required for use of the JC material model. This common curve will be used in subsequent evaluations of the JC material model. As shown in appendix A, the functional dependence of stress on strain at constant strain rate and temperature can be represented very well by a power law equation, as required by the JC material model.

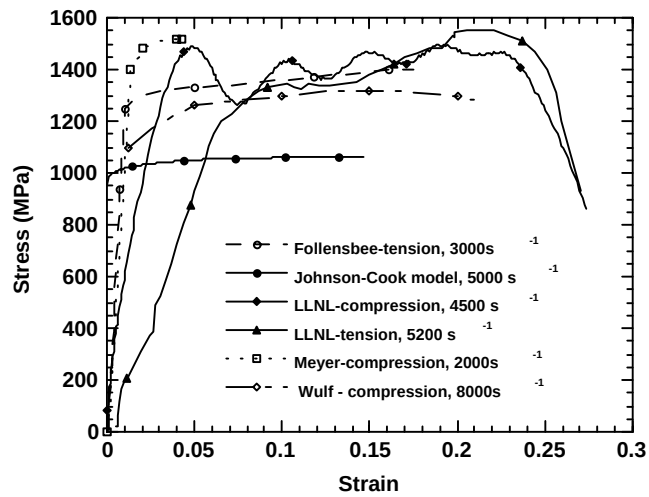

FIGURE 10. COMPARISON OF THE HIGH-STRAIN RATE, STRESS-STRAIN RESPONSE OF THE Ti-6Al-4V ALLOY IN TENSION AND COMPRESSION

NOTES: 1. Data is also provided for other high-rate studies of annealed Ti-6Al-4V from the literature. The predictions of the Johnson-Cook material model using the original parameters are shown in the figure.

2. Literature data plotted in the figure are described in table 4.

It is useful to compare the results of the present study with stress-strain data obtained on "hot worked" and "annealed" Ti-6Al-4V by other investigators. Four high-strain rate studies, which are of interest, are shown in table 4. The type of tests conducted, material processing history, and microstructure (as described by the investigators) are indicated in the table. The stress-strain data from these studies are compared with data from the present study in figure 10. The strain rates ranged from 2000 s^{-1} to 8000 s^{-1}. At large strains (greater than a strain of .05), the flow stress

data for the five investigations agree within about 100 MPa. The data for all studies fall within a tight band with a range of about 100 MPa. Of particular note is the investigation by Wulf [18], who studied Ti-6Al-4V processed to the AMS 4911 specification. The materials, whose data appear in figure 10, were all processed using hot working and annealing procedures similar to the procedures prescribed in AMS 4911. Thus, it appears that, despite slightly different compositions and processing histories, only relatively minor variations in the high-strain rate, stress-strain behavior result. At quasi-static strain rates, the stress-strain response of Ti-6Al-4V is influenced by microstructure, composition (including interstitial content), and texture with variations of 200 MPa possible [16].

TABLE 4. HIGH-RATE LITERATURE DATA FOR ANNEALED Ti-6Al-4V

Investigators	Type of Tests	Material Processing History/ Microstructure	Ref.
Follansbee and Gray	Hopkinson bar (compression)	Hot-rolled plate Equiaxed α (5 μm grain size) with β at grain boundary triple points	[19]
Meyer	servohydraulic (tension and compression); impact pendulum (tension); rotating wheel (tension); drop weight (compression)	Hot-rolled bar, heat treated at 700°C, 2 hr, air cooled Globular α	[20]
Wulf	modified Hopkinson bar (compression)	AMS 4911B	[18]
Lee and Lin	Hopkinson bar (compression) Tests done at 25, 700, 900, 1100°C	Hot extruded bar	[21]
Johnson	Quasi-static tension; Torsion; Hopkinson bar (tension)	Unknown	[22, 23]

Stress-strain rate data obtained from the various studies are shown in figure 11 on a semilog plot. All data was obtained at a strain of 0.04 with the exception of the study by Wulf, which was obtained at a strain of 0.1. Below a strain rate of about 10^3 s^{-1}, the data follows a straight line. Thus, at these lower strain rates, there is a logarithmic dependence of stress on strain rate as required by the JC material model. The logarithmic dependence of stress on strain rate is fundamentally justified in that obstacle-controlled plasticity, which is expected to dominate at low stresses and temperatures, has a logarithmic dependence of stress on strain rate [24]. At strain rates greater than 10^3 s^{-1}, however, the data shows a dramatic increase in strength with strain rate that cannot be accounted for with this logarithmic dependence. This increase in strength has been observed in a number of metals (see, for example reference 25) and is generally recognized as resulting from a change in deformation mechanism. At lower strain rates, the deformation rate is controlled by the cutting or bypassing of discrete obstacles by dislocations. At higher rates, the deformation rate is controlled by phonon or electron drag on moving dislocations. These two mechanisms are represented by different deformation rate equation [26], which produce the dramatic change in behavior on going from low strain rates to high strain

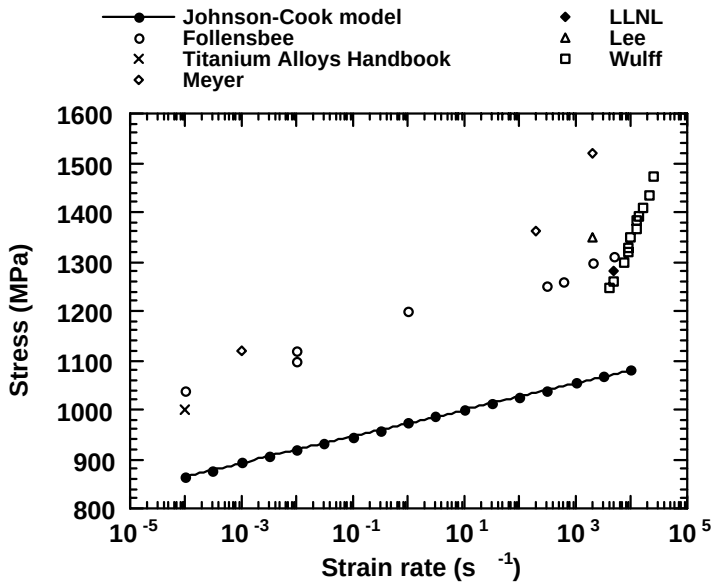

FIGURE 11. COMPARISON OF THE STRESS-STRAIN RATE RESPONSE OF Ti-6Al-4V ALLOY OBTAINED FROM THIS STUDY AS WELL AS OTHER STUDIES FROM THE LITERATURE

NOTES: 1. All data was obtained at a strain of 0.04 with the exception of the study by Wulf, which was obtained at a strain of 0.1. The predictions of the Johnson-Cook material model using the original parameters are also shown in the figure.

2. Literature data plotted in the figure are described in table 4.

rates. Such dramatic changes in behavior are outside the scope of the JC model. In our derivation of material parameters for the JC model, we confine our study to stress-strain rate data below strain rates of 10^3 - 10^4 s^{-1}.

It is important to recognize that at quasi-static strain rates (e.g., 10^{-4} s^{-1}), the Ti-6Al-4V alloy is well known for exhibiting the so-called "strength differential effect", in which the flow stress in compression is higher than the flow stress in tension. The difference in flow stress can be quite large. For example, Lowden and Hutchinson [27] have reported that for Ti-6Al-4V annealed at 930°C and air cooled (microstructure consisted of primary alpha and transformed beta), the flow stress in the rolling direction was approximately 100 MPa higher in compression than tension. In the transverse direction, the difference in flow stress could be as large as 900 MPa. Chait [28] has also reported a strength differential effect in Ti-6Al-4V. In this study, samples were annealed at 750°C, and the difference in yield strength between tension and compression was about 85 MPa. However, in work by Meyer on hot-rolled and annealed Ti-6Al-4V [20], the strength differential effect was virtually absent. In the current study, tests were done at strain rates of 10^{-3} s^{-1} and 200 s^{-1} and the maximum flow stress difference between tension and compression was less than 20 MPa. The observation of a strength differential effect appears to be very sensitive to relatively small variations in composition and processing.

3.2 DATA FOR 2024-T3 ALUMINUM.

3.2.1 Stress-Strain Data for 2024-T3.

3.2.1.1 Compression for 2024-T3.

The true stress-true strain response for the 2024-T3 alloy in compression is shown in figure 12. The nominal strain rate in these tests was 4000 s^{-1}. Two tests are shown for each of the three testing orientations evaluated and the repeatability of the test data is excellent. As shown in the figure, both samples tested in the in-plane 0° orientation had flow stresses that were slightly lower than the flow stresses for the in-plane 90° and normal orientations (maximum deviation was 20 MPa). This deviation between stress-strain curves is very small and thus the stress-strain response can be considered isotropic. This is an important finding, since the JC material model assumes isotropic behavior. As mentioned in section 3.1, the oscillations in the stress-strain curves are the result of obtaining data from the long elastic pressure bars. The stress-strain response of the sample is considerably more uniform and can be taken as the average curve through the data in figure 12. For the 2024-T3 samples tested in compression, the fracture strain could not be determined. The maximum strains shown for the stress-strain curves in figure 12 represent the limits at which reliable data were obtained. The samples deformed considerably more, after the maximum strains shown in the figure, without obvious fracture or dramatic loss in load bearing capability. The maximum strains obtained in figure 12 are recorded in table 3.

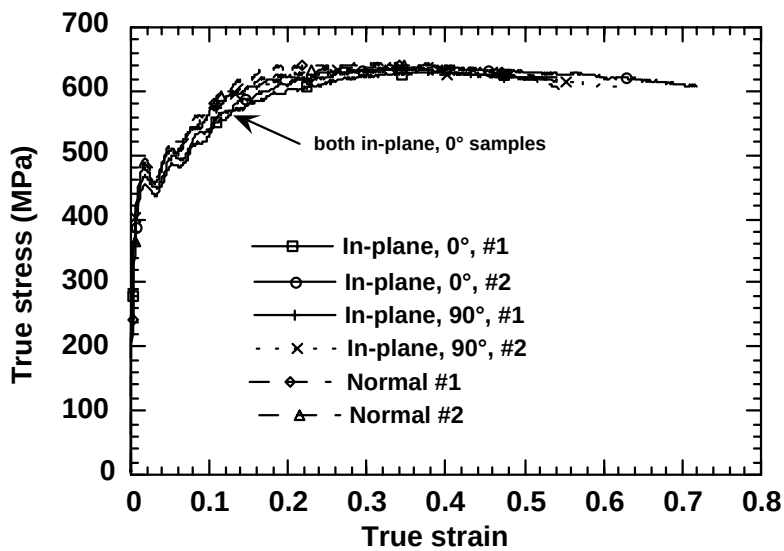

FIGURE 12. STRESS-STRAIN RESPONSE FOR 2024-T3 ALLOY TESTED IN COMPRESSION AT A STRAIN RATE OF 4000 s^{-1}

3.2.1.2 Tension for 2024-T3.

The true stress-true strain response for the 2024-T3 alloy in tension is shown in figure 13. The nominal strain rate in these tests was 8000 s^{-1}. Test results are shown for both in-plane orientations. The data for the two orientations virtually superimpose demonstrating that the

tensile stress-strain response in the plane is isotropic. As discussed in section 3.1, the stress-strain curves shown in figures 12 and 13 can be considered valid, once the samples have yielded plastically, which is accompanied by stress and strain rate uniformity in the sample.

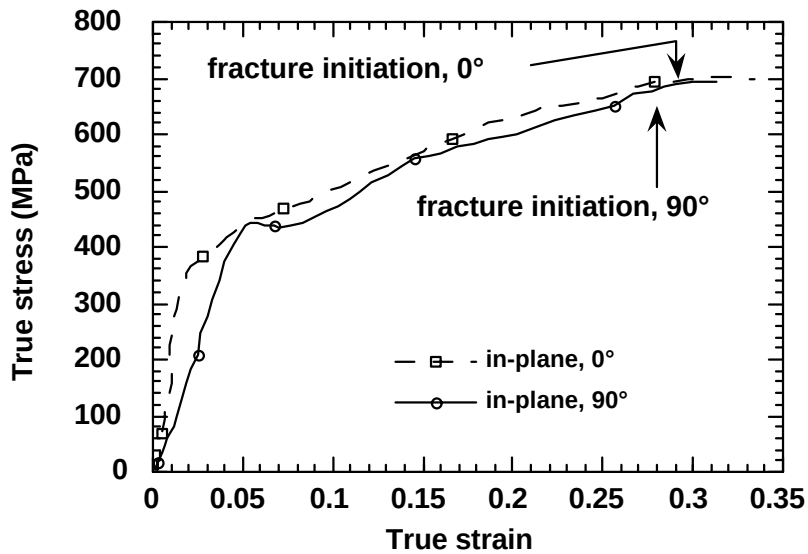

FIGURE 13. STRESS-STRAIN RESPONSE FOR 2024-T3 ALLOY TESTED IN TENSION AT A STRAIN RATE OF 8000 S^{-1}

3.2.2 Microstructural Characterization.

As shown in figure 12, the 2024-T3 compression samples deformed to very large strains during testing. The deformation in these samples was so large that meaningful posttest characterization of the compression samples was not possible. The tensile samples had several interconnected shear fractures in a given sample. Examination of the framing camera records revealed that the tensile samples failed, without noticeable necking, by initiation of cracking at the corners of the sample. The strains at which fracture was initiated are indicated in figure 13 and recorded in table 3. For both tensile samples studied, fracture initiated at the maximum stress as shown on the stress-strain curves in figure 13.

3.2.3 Data Analysis.

Stress-strain curves in tension and compression for the 2024-T3 alloy are plotted on a common set of axes in figure 14. The tensile stress-strain curves include data obtained in both in-plane orientations. The results show that, in the region of valid data (large-scale plastic flow), the three curves coincide. Thus, the stress-strain behavior of the 2024-T3 alloy is insensitive to the sign of the applied stress (tension versus compression). In section 3.2.1 we noted that the material is also extremely isotropic. Thus, we will assume that the stress-strain behavior of the 2024-T3 alloy is isotropic and insensitive to mean stress, which is required for use of the JC material model.

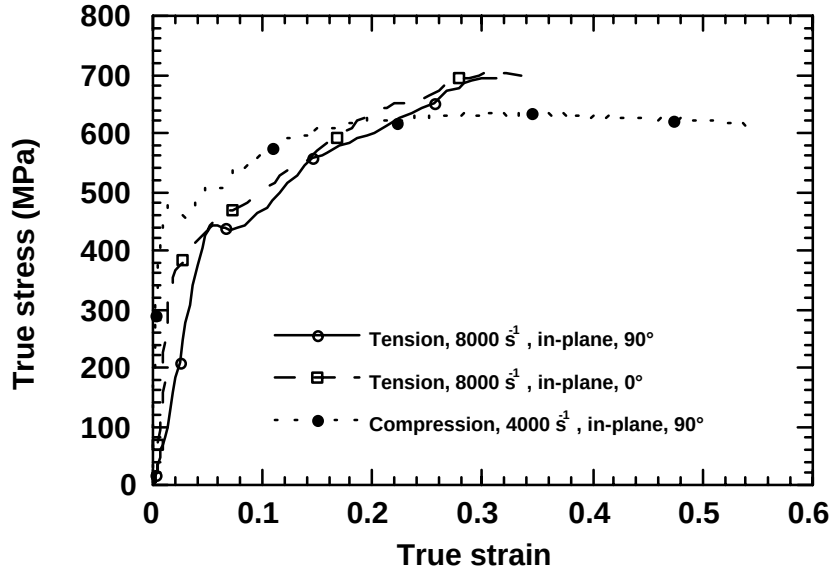

FIGURE 14. COMPARISON OF THE HIGH-STRAIN RATE, STRESS-STRAIN RESPONSE OF 2024-T3 ALLOY IN TENSION AND COMPRESSION

The stress-strain curves in compression show a maximum stress at a strain of about 0.3. O'Donnell and Woodward [29] have estimated the thermal softening in the 2024 alloy due to adiabatic heating, and found that a maximum in the stress-strain curve is expected at a strain of 0.27. Thus, the maximum shown in the stress-strain curves in figure 12 should be associated with adiabatic heating effects and not associated with the initiation of an instability (shear bands). Previous studies of shear localization have shown that a maximum in the stress-strain curve is a necessary but not sufficient condition for shear localization, Semiatin et al. [30, 31]. Indeed, noticeable amounts of shear softening must occur before flow localization occurs.

The data reported here represent the first published studies of the high-rate, stress-strain response of 2024-T3. Data have been reported for the 2024 alloy in the T351 temper [10, 29, 32]. Both the T3 and T351 tempers designate material that has been solution heat-treated, cold-worked, and naturally aged. The T3 temper applies to flat sheet material that is less than 6.3 mm thick; whereas the T351 temper applies to plate material that is greater than 6.3 mm thick. For plate thickness less than 51 mm thick, data reported in the Aerospace Structural Metals Handbook [33] and the Source Book on Industrial Alloy and Engineering Data [34] show that the yield and ultimate tensile strengths in the two tempers are virtually identical. Data taken on 2024-T351 are thus a valuable source of information for our analysis of the 2024-T3 alloy. Shear stress-shear strain data on the 2024-T351 alloy in torsion has been reported by Johnson et al. [10], Lindholm and Johnson [32], and Johnson and Holmquist [23] for shear strain rates from 0.088 s^{-1} to 123 s^{-1}. Each of these references reports the same data set, which consists of six torsion tests. The parameters for the JC material model reported in the next section were derived from these six tests on the 2024-T351 alloy.

O'Donnell and Woodward have studied the development of shear bands in 2024-T351 plate during compression testing [29]. A drop weight tower was used and initial strain rates of 600 s^{-1} were obtained. Tests were conducted in the rolling (0°), transverse (90°), and through the thickness directions (normal) at temperatures from 0°C to 90°C. The strains at which instabilities were observed (drops in the in the load-displacement records) are reported in table 5 for the tests conducted at 20°C. These instabilities were associated with intense shear bands and cracking within these bands. For practical purposes, these strains can be considered as failure strains for the 2024-T351 alloy in compression, since sufficient flow localization and cracking occurred to cause abrupt losses in loading bearing capacity. The variations in the instability strains can be attributed to the inherent inhomogeneous distribution of inclusions, which are the origins of fracture, as well as variations in shear bandwidth.

TABLE 5. INSTABILITY STRAINS FOR 2024-T351 IN COMPRESSION [24]

Orientation	Test	Instability Strain
0° (rolling direction)	1	0.87
90° (transverse direction)	1	0.79
	2	0.74
Through thickness (normal)	1	0.76
	2	0.70
	3	0.70
	4	0.85

4. ANALYSIS OF JOHNSON-COOK MATERIAL MODEL.

The JC parameters for the Ti-6Al-4V alloy were reported by Johnson [22] as part of a study for the Naval Surface Weapons Center (NSWC). The parameters are provided in table 6. The parameters were based on eight torsion tests, four Hopkinson bar tests and two quasi-static tensile tests. In figure 15, the stress-strain rate curve predicted from the JC model at a strain of 0.002 is compared to some of the original data reported by Johnson and Myers [23, 24]. The rapid increase in strength at the higher strain rates mentioned in section 3.1.3 is evident in this data set. The torsion data (provided as shear stress versus shear strain at several shear-strain rates) was converted to effective (Von Mises) quantities using the following expressions

$$\sigma = \sqrt{3}\tau \tag{6}$$

$$\varepsilon = \gamma / \sqrt{3} \tag{7}$$

$$\dot{\varepsilon} = \dot{\gamma} / \sqrt{3} \tag{8}$$

TABLE 6. ORIGINAL PARAMETERS FOR JOHNSON-COOK MATERIAL MODEL

	A (MPa)	B (MPa)	n	C	m	D_1	D_2	D_3	D_4	D_5
Ti-6Al-4V	862	331	0.34	0.012	0.8	-0.09	0.25	-0.5	0.014	3.87
2024-T351	265	426	0.34	0.015	1	0.13	0.13	-1.5	0.011	0.0

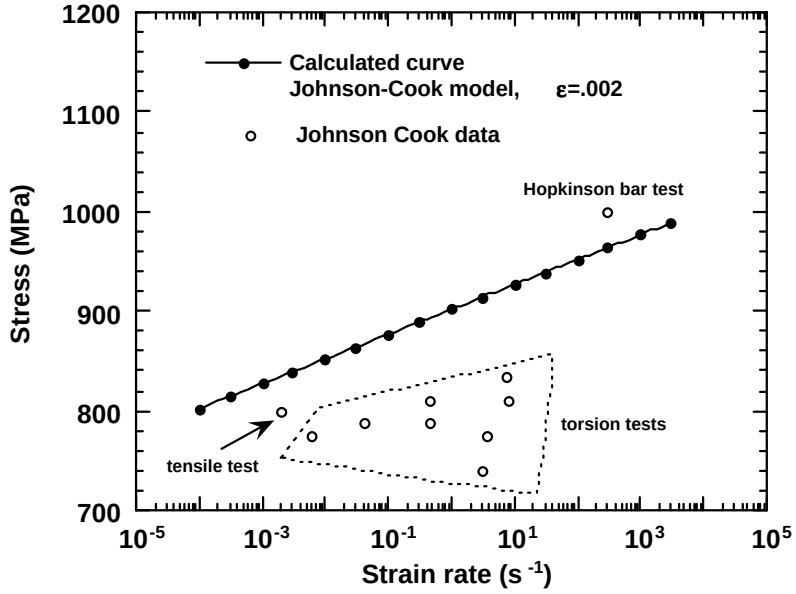

FIGURE 15. STRESS-STRAIN RATE DATA OBTAINED BY JOHNSON FOR THE Ti-6Al-4V ALLOY AT A PLASTIC STRAIN OF 0.002

NOTE: The predictions of the Johnson-Cook model using the original parameters are also shown in the figure.

In reference 23, the Ti-6Al-4V alloy was identified as having been "provided by NSWC." No processing history or microstructural characterization was provided in the report. However, the hardness was quoted as Rc 29, which is extremely low for Ti-6Al-4V. A typical hardness value for the Ti-6Al-4V alloy processed to the AMS 4911 specification would be Rc 36 [35]. The parameters for the JC model reported by Johnson reflect the low hardness (strength) of the alloy that was evaluated. The predicted adiabatic stress-strain curve was calculated using equations 1, 2, and 3, assuming that 100% of the plastic work is transformed into heat ($\alpha = 1$). The physical properties used in these calculations are shown in table 7. The predicted adiabatic stress-strain response at a strain rate of 5000 s^{-1} using these original set of JC parameters was shown in figure 10. As expected, the predicted stress-strain curve was significantly softer than any of the experimental data for annealed Ti-6Al-4V. The stress-strain rate response predicted by the JC model was shown in figure 11 for a strain of 0.04. The calculations were done using the original JC parameters provided in table 6. The predicted curve is significantly softer than experimental data. In addition, the model was unable to capture the rapid increase in strength at the high strain rates.

TABLE 7. PHYSICAL PROPERTIES OF Ti-6Al-4V AND 2024-T3

	Melting Temperature (°C) [reference]	Density (kg/m^3) [reference]	Heat Capacity (J/kg K) [reference]
Ti-6Al-4V	1605 [11]	4428 [11]	580 [11]
2024-T3	502 [28]	2770 [28]	875 [28]

The original JC parameter for the 2024-T351 alloy [10, 32] were determined on the basis of six torsion tests with strain rates ranging from 0.088 s^{-1} to 123 s^{-1}. These parameters are provided in table 6. In the next section, a new set of JC parameters are provided and evaluated for the strength component of the JC model for both Ti-6Al-4V and 2024-T3.

5. NEW CONSTANTS FOR JOHNSON-COOK MATERIAL MODEL.

5.1 Ti-6Al-4V TITANIUM.

New sets of parameters for both Ti-6Al-4V and 2024-T3 were determined for the strength component of the JC model using the procedures outlined in appendix A. For both alloys, the A, B, and n parameters were determined using the current Hopkinson bar data. Data from the literature and the current data were used to determine C and m. The new parameters are provided in table 8. The predictions of the JC model for Ti-6Al-4V with these new constants are compared with experimental data in figure 16-19. Figures 16 and 17 compare the stress-strain response with experimental data at a high-strain rate and a low-strain rate, respectively. The low rate data were obtained from the Ti Alloys Handbook [36]. Figures 18 and 19 compare the stress-strain rate response and the stress-temperature response, respectively, with experimental data. The stress-temperature response was considered at both high-strain rates (2500 s^{-1}) and low-strain rates (10^{-4} s^{-1}). The high-rate data were obtained from the work of Lee and Lin [21] at three strains and the low-rate data were obtained from the Aerospace Structural Materials Handbook [37] and the Titanium Alloys Handbook [36]. The stress versus temperature data are provided in figure A-3 and the high rate data were used to establish the m parameter.

TABLE 8. NEW PARAMETERS FOR JOHNSON-COOK MATERIAL MODEL

	A (MPa)	B (MPa)	n	C	m	D_1	D_2	D_3	D_4	D_5
Ti-6Al-4V	1098	1092	0.93	0.014	1.1	-0.09	0.25	-0.50	0.014	3.87
2024-T3	369	684	0.73	0.0083	1.7	0.13	0.13	-1.5	0.011	0.0

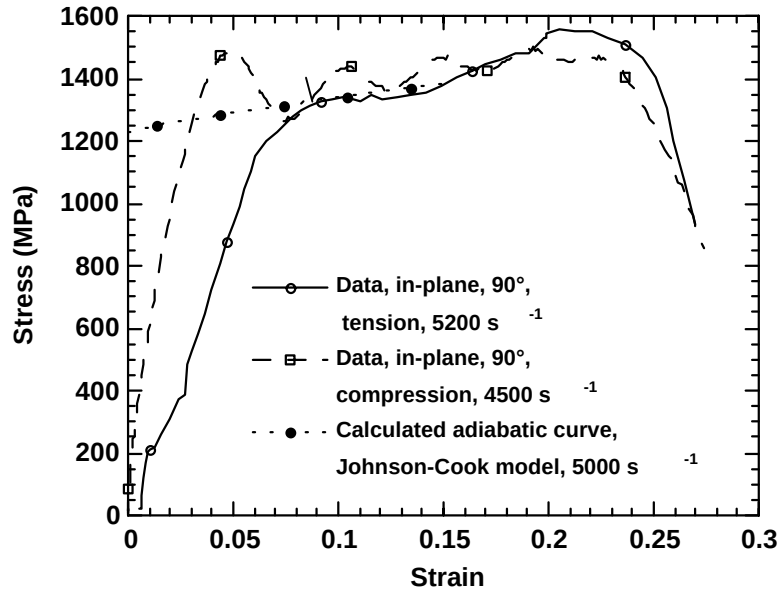

FIGURE 16. COMPARISON OF THE HIGH-STRAIN RATE, STRESS-STRAIN RESPONSE OF THE Ti-6Al-4V ALLOY PREDICTED BY THE JOHNSON-COOK MATERIAL MODEL (USING THE NEW MATERIAL PARAMETERS) WITH EXPERIMENTAL DATA IN TENSION AND COMPRESSION

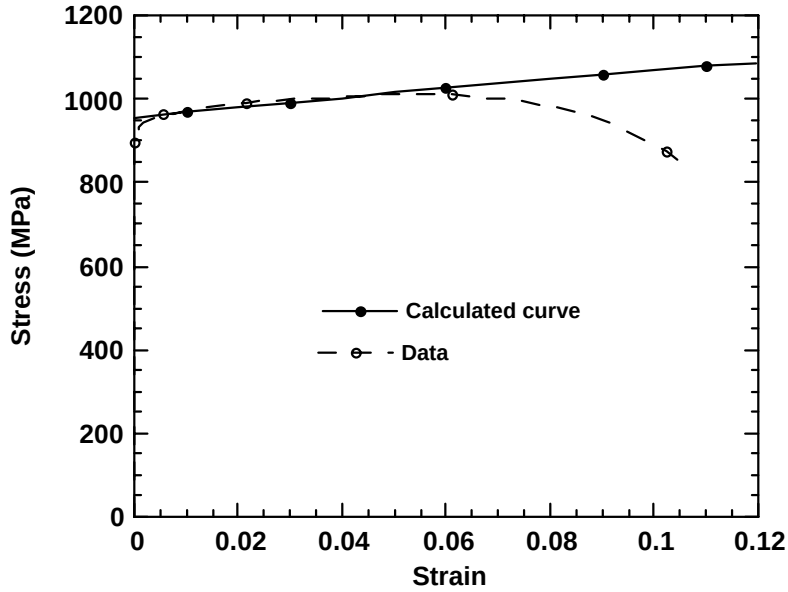

FIGURE 17. COMPARISON OF THE LOW-STRAIN RATE (0.0001 S^{-1}), STRESS-STRAIN RESPONSE OF THE Ti-6Al-4V ALLOY AS PREDICTED BY THE JOHNSON-COOK MATERIAL MODEL (USING THE NEW MATERIAL PARAMETERS) WITH EXPERIMENTAL DATA IN TENSION

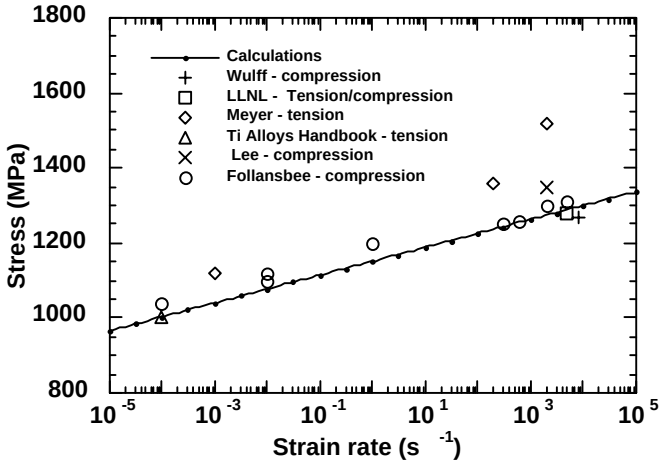

FIGURE 18. COMPARISON OF THE STRESS-STRAIN RATE RESPONSE OF THE Ti-6Al-4V ALLOY AS PREDICTED BY THE JOHNSON-COOK MATERIAL MODEL (USING THE NEW MATERIAL PARAMETERS) WITH EXPERIMENTAL DATA. CALCULATIONS AND DATA WERE TAKEN AT A STRAIN OF 0.04.

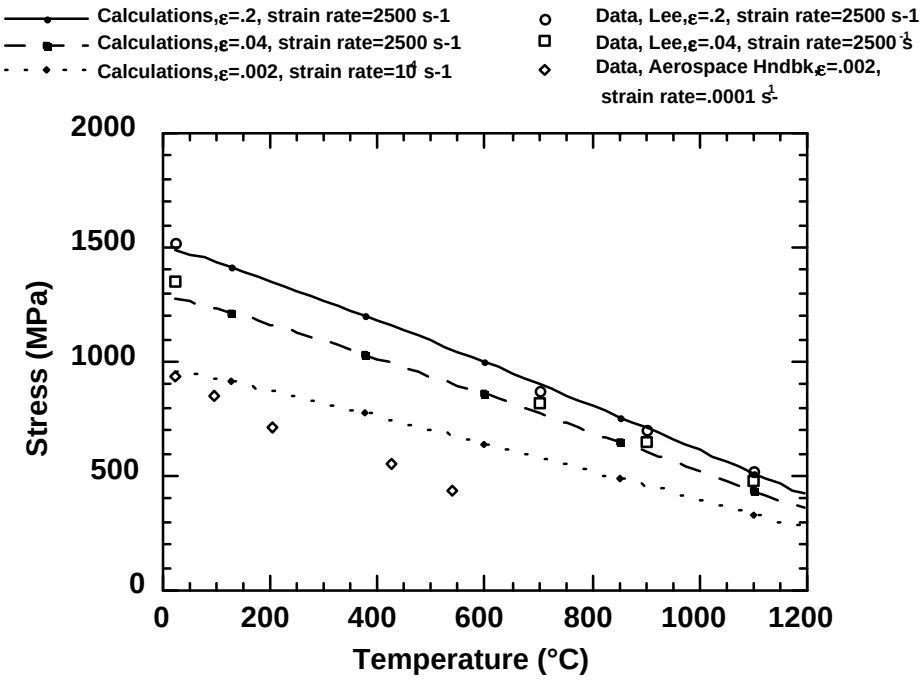

FIGURE 19. COMPARISON OF THE STRESS-TEMPERATURE RESPONSE OF THE Ti-6Al-4V ALLOY AS PREDICTED BY THE JOHNSON-COOK MATERIAL MODEL (USING THE NEW MATERIAL PARAMETERS) WITH EXPERIMENTAL DATA

Examination of figures 16-19 provides the following assessment of the capabilities and limitations of the strength component of the JC model with the new parameters.

a. Stress-Strain Behavior: The model can accurately represent the yield and plastic flow behavior of Ti-6Al-4V at both low- and high-strain rates with a single set of material constants. The model does not account for anisotropy which can produce flow stress differences of approximately 250 MPa (figure 3) in Ti-6Al-4V processed to the AMS 4911 specification. However, anisotropy was only observed in the 90° orientation, compression experiments. Other orientations and testing modes showed isotropic behavior. For practical utilization of this material model, limitations resulting from anisotropy are considered to be relatively minor.

b. Stress-Strain Rate Behavior: Below a strain rate of 10^3 s^{-1}, the model can adequately represent the stress-strain rate response of the alloy. Above 10^3 s^{-1}, flow stresses can increase sharply with increasing strain rate due to a change in deformation mechanism as discussed in section 3.1.3. These higher strain rates are of primary interest to simulations involving engine containment and the influence of uncontained engine debris on aircraft structures. Examination of figure 18 suggests that the strain rate at which the rapid increase in flow stresses occurs is sensitive to composition and processing. For the data of Wulf (processed to the AMS 4911 specification), the model predicts flow stresses at a strain rate of 20,000 s^{-1} that are about 150 MPa low.

c. Stress-Temperature Behavior: Figure 19 shows that at high-strain rates the stress-temperature response can be represented very well by the model. At low-strain rates, however, the model predicts stresses that are significantly higher than observed experimentally (e.g., 250 MPa high at 500°C). Clearly the temperature term is influenced by strain rate (or stress). Other constitutive equations, such as in the mechanical threshold stress model, account for the influence of stress on thermal activation and thus temperature dependence. For our purposes, the JC model can be considered adequate if the m parameter is evaluated in the high strain rate range.

The adiabatic stress-strain response for Ti-6Al-4V at 5000 s^{-1} predicted by the JC material model using the new strength parameters is shown in figure 20. Results are shown for loading in tension, shear, and compression. The predicted failure strains and resulting temperature rise in the sample are shown in the figure. The calculations assume uniform deformation and 100% of the mechanical work is dissipated as heat. The results predict a 110°C increase in temperature in tension and 140°C increase in temperature in compression. The failure strains observed in the Hopkinson bar tests for Ti-6Al-4V (reported in table 3) show that at high-strain rates (about 5000 s^{-1}) the failure strain is independent of pressure and equal to 0.2. The results in figure 20 show that the failure strains predicted with the damage constants given in table 8 have a mild pressure dependence. A better representation of the experimental data would thus be obtained if the damage parameter D_2 were 0. A complete analysis of failure would require consideration of the failure mode (shear localization) as well as the influence of strain rate and temperature. Failure in the Ti-6Al-4V alloy needs to be considered further.

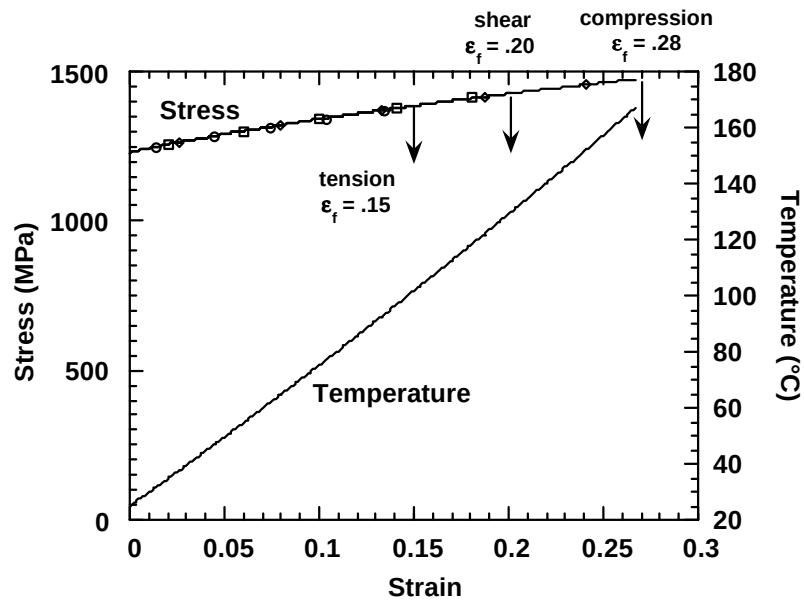

FIGURE 20. PREDICTED ADIABATIC STRESS-STRAIN RESPONSE FOR THE Ti-6Al-4V ALLOY IN TENSION, SHEAR, AND COMPRESSION AT A STRAIN RATE OF 5000 S^{-1}

NOTE: The predicted failure strains and resulting temperature rise in the sample are shown in the figure.

5.2 2024-T3 ALUMINUM.

The predictions of the JC model for 2024-T3 with the new constants are compared with experimental data in figures 21-24. Figures 21 and 22 compare the stress-strain response with experimental data at a high-strain rate and a low-strain rate, respectively. The low-rate data were obtained from the Aerospace Structural Materials Handbook [37] and the ASM International Handbook [38]. Figures 23 and 24 compare the stress-strain rate response and the stress-temperature response, respectively, with experimental data. Data for the stress-temperature response was available at low-strain rates (10^{-4} s^{-1}) only [38]. The results in figures 21-24 show that the strength component of the JC model with the new parameters can predict the stress-strain rate and the stress-temperature response of 2024-T3 very well. The major concern with the JC model is its ability to accurately represent the stress-strain rate response of 2024-T3 at higher-strain rates than studied here. Theory predicts that, as with Ti-6Al-4V, the stress will increase sharply at higher-strain rates (e.g., greater than 10^4 s^{-1}) in a manner that can not be accounted for by the logarithmic dependence of stress on strain rate that is shown in figure 23. Indeed, work with other aluminum alloys (e.g., 6061-T6 [39]) has shown that sharp increases in strength are observed at strain rates greater than 10^3 s^{-1}.

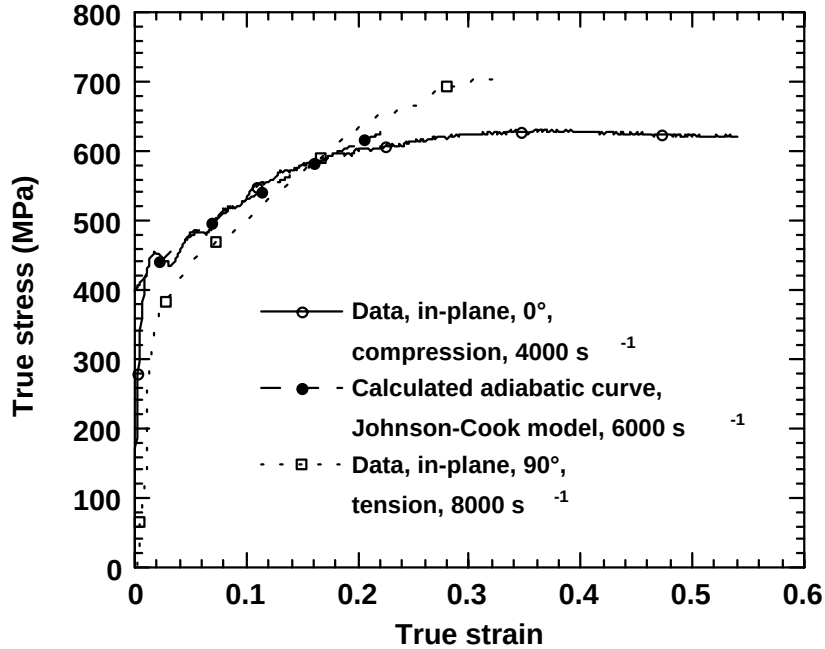

FIGURE 21. COMPARISON OF THE HIGH-STRAIN RATE, STRESS-STRAIN RESPONSE OF THE 2024-T3 ALLOY PREDICTED BY THE JOHNSON-COOK MATERIAL MODEL (USING THE NEW MATERIAL PARAMETERS) WITH EXPERIMENTAL DATA INTENSION AND COMPRESSION

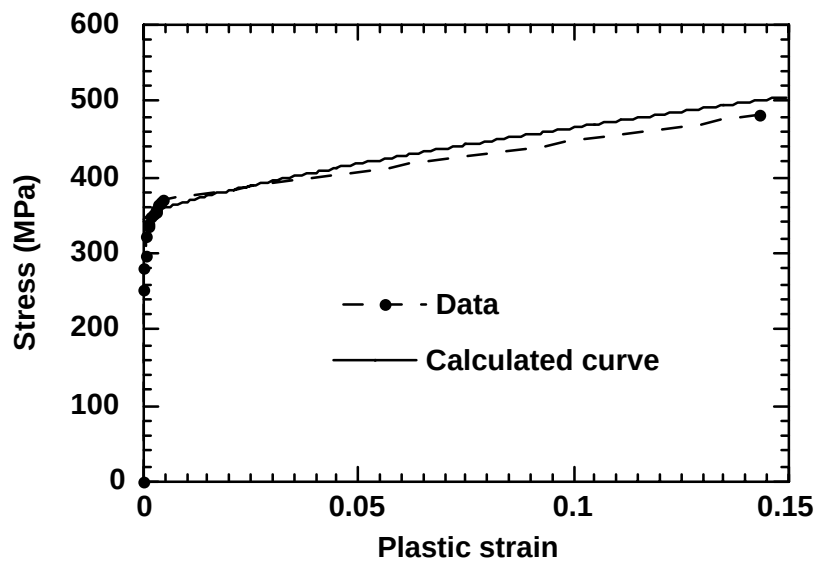

FIGURE 22. COMPARISON OF THE LOW-STRAIN RATE (0.0005 S^{-1}), STRESS-STRAIN RESPONSE OF THE 2024-T3 ALLOY AS PREDICTED BY THE JOHNSON-COOK MATERIAL MODEL (USING THE NEW MATERIAL PARAMETERS) WITH EXPERIMENTAL DATA IN TENSION

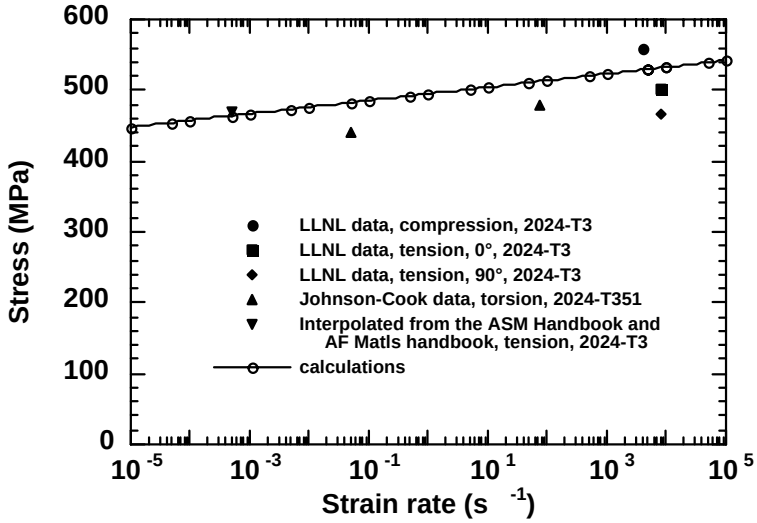

FIGURE 23. COMPARISON OF THE STRESS-STRAIN RATE RESPONSE OF THE 2024-T3 ALLOY AS PREDICTED BY THE JOHNSON-COOK MATERIAL MODEL (USING THE NEW MATERIAL PARAMETERS) WITH EXPERIMENTAL DATA

NOTE: Calculations and data were taken at a strain of 0.1.

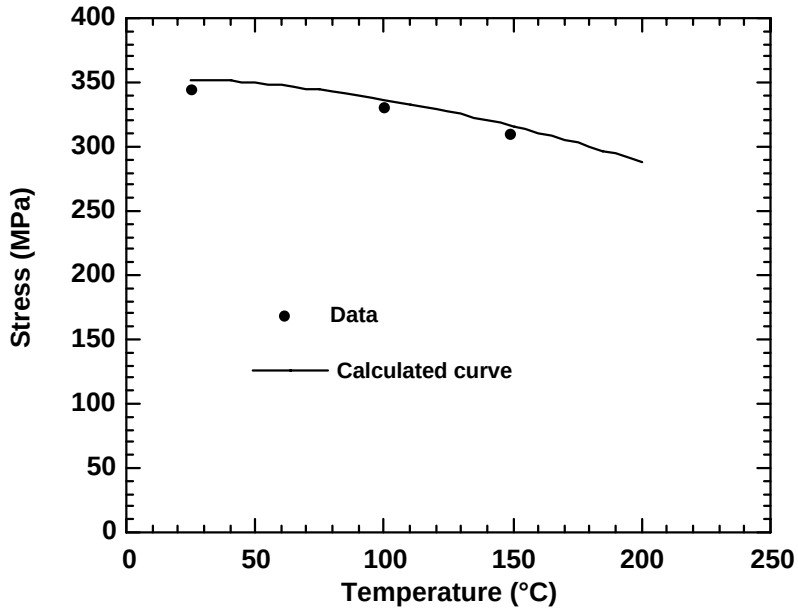

FIGURE 24. COMPARISON OF THE STRESS-TEMPERATURE RESPONSE OF THE 2024-T3 ALLOY AS PREDICTED BY THE JOHNSON-COOK MATERIAL MODEL (USING THE NEW MATERIAL PARAMETERS) WITH EXPERIMENTAL DATA

NOTE: Calculations and data were taken at a strain rate of .0005 s^{-1} and a strain of 0.002.

The adiabatic stress-strain response for 2024-T3 at 6000 s^{-1} predicted by the JC material model using the new strength parameters is shown in figure 25. Results are shown for loading in tension, shear, and compression. The predicted failure strains and resulting temperature rise in the sample are shown in the figure. The calculations assume uniform deformation and 100% of the mechanical work is dissipated as heat. The results predict a 70°C increase in temperature in tension and 90°C increase in temperature in compression. Tables 3 and 5 show that, for the 2024-T3 alloy, failure in tension occurs at a strain of 0.3, whereas failure in compression occurs at a strain of 0.8. Thus, the experimental data at high-strain rates show a much stronger pressure dependence than shown in figure 25. The damage parameters used in these calculations were established by Lindholm and Johnson [32] and Johnson, Hoegfeldt, and Nagy [10] on the basis of torsion tests only with strain rates from 0.088 s^{-1} to 123 s^{-1}. As with the Ti-6Al-4V alloy, a complete analysis of failure would require consideration of the failure mode (shear localization). Failure in the 2024-T3 alloy needs to be considered further.

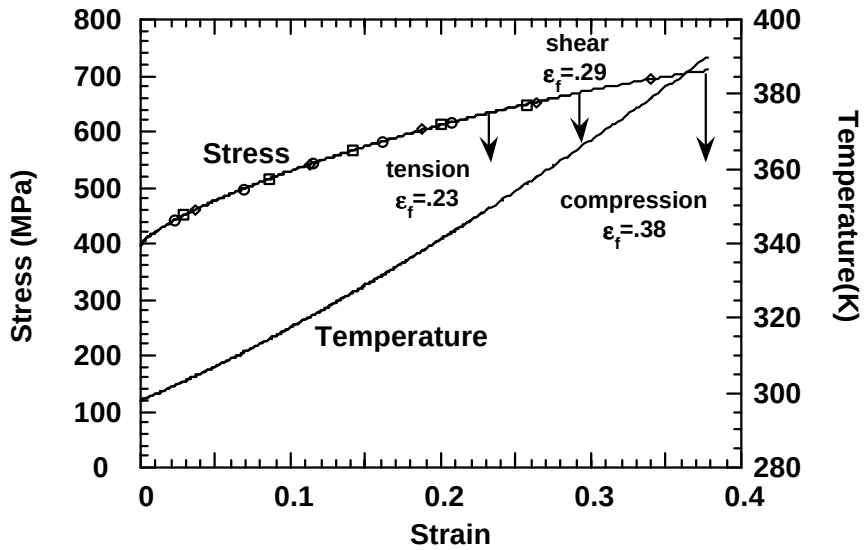

FIGURE 25. PREDICTED ADIABATIC STRESS-STRAIN RESPONSE FOR THE 2024-T3 ALLOY IN TENSION, SHEAR, AND COMPRESSION AT A STRAIN RATE OF 6000 s^{-1}

NOTE: The predicted failure strains and resulting temperature rise in the sample are shown in the figure.

6. SUMMARY.

The high-strain rate, large strain deformation, and fracture response of Ti-6Al-4V and 2024-T3 were evaluated using the split Hopkinson pressure bar technique. Both materials were processed to specifications appropriate for aircraft and engine designs. Stress vs. strain and stress vs. strain rate (generated in the current study) and additional data from the literature were used to critically evaluate the ability of the JC model to represent the deformation and failure response of these materials under conditions relevant to simulations of engine containment and the influence of uncontained engine debris on aircraft structures. The results were used to define a new set of

material constants for the JC model. For both materials, fracture occurred by shear localization. For Ti-6Al-4V, fracture features observed in the Hopkinson bar samples were comparable to fracture features observed during postfailure analysis of a Ti-6Al-4V fan case, which was impacted by a fan blade. Both failures occurred by shear localization.

The results and analysis provided for both Ti-6Al-4V and 2024-T3 show that the JC model can accurately represent the stress-strain response of the materials. Other aspects of material behavior, such as plastic anisotropy and the influence of temperature, are not expected to adversely affect the use of the material model for high-strain rate deformation and fracture problems. A concern with the JC material model is its ability to accurately represent the stress-strain rate response at strain rates greater than approximately $10^4 s^{-1}$. For both materials, the deformation mechanism changes. The mechanisms at low-strain rate and high-strain rate are represented by different deformation rate equations, which predict a dramatic change in behavior in going from low-strain rates to high-strain rates. Such dramatic changes in behavior are outside the scope of the JC model. It is believed that the JC models, with new parameters, adequately represents the bulk of the deformation response for problems of interest to this program. LLNL is continuing to investigate the influence of the high-strain rate effects described above. This report provides new strength parameters for the JC model and does not address the failure parameters. Determination of the failure parameters is underway and will be addressed in a future report. Both sets of parameters are needed for adequate simulation of penetration and perforation performance. The models and damage constants available in the literature also do not predict the correct failure strains.

7. REFERENCES.

1. R.G. Whirley and B.E. Englemann, DYNA3D User Manual, UCRL-MA-107254 Rev. 1, November 1993.

2. Johnson, G. R. and W. H. Cook, "A Constitutive Model and Data for Metals Subjected to Large Strains, High Rates and High Temperatures," in *Proceedings of the Seventh International Symposium on Ballistics*, The Netherlands, The Hague, pp. 541-547, 1983.

3. Johnson, G. R. and T. J. Holmquist, "Evaluation of Cylinder-Impact Test Data for Constitutive Model Constants," *Journal of Applied Physics*, Vol. 64, No. 8, pp. 3901-3910, 1988.

4. G. R. Johnson and W. H. Cook, "Fracture Characteristics of Three Metals Subjected to Various Strains, Strain Rates, Temperatures and Pressures," *Engineering Fracture Mechanics*, Vol. 21, No. 1, pp. 31-48, 1985.

5. Zerilli, F. J. and R. W. Armstrong, "Dislocation-Mechanics-based Constitutive relations for Material Dynamics Calculations," *Journal of Applied Physics*, Vol. 61, No. 5, pp. 1816-1825, 1987.

6. Zerilli, F. J. and R. W. Armstrong, "Description of Tantalum Deformation Behavior by Dislocation Mechanics Based Constitutive Equations," *Journal of Applied Physics*, Vol. 68 No. 4, pp. 1580-1591, 1990.

7. Zerilli, F. J. and R. W. Armstrong, "The Effect of Dislocation Drag on the Stress-Strain Behavior of FCC Metals," *Acta Metallurgica et Materialia*, Vol. 40, No. 8, pp. 1803-1808, 1992

8. Steinberg, D. J., S. G. Cochran, and M. W. Guinan, "A Constitutive Model for Metals Applicable at High-Strain Rate," Lawrence Livermore National Laboratory, UCRL-80465, Revision 2, 1979.

9. Follansbee, P. S. and U. F. Kocks, "A Constitutive Description of the Deformation of Copper Based on the use of the Mechanical Threshold Stress as an Internal State Variable," *Acta Metallurgica*, Vol. 36, pp. 81-93, 1988.

10. Johnson, G. R., J. M. Hoegfeldt, U. S. Lindholm, and A. Nagy, "Response of Various Metals to Large Torsional Strains over a Large Range of Strain Rates—Part 2: Less Ductile Metals," *Journal of Engineering Materials and Technology, Transactions of the ASME*, Vol 105, pp. 48-5, 1983.

11. P.S. Follansbee, "The Hopkinson Bar," in Metals Handbook, Ninth Edition, Volume 8, Mechanical Testing, 198-203. 1985.

12. M.M. LeBlanc and D.H. Lassila, "Dynamic Tensile Testing of Sheet Material Using the Split Hopkinson Bar Technique," Experimental Techniques, Vol. 17, No. 1, 37-42 (1993).

13. Conrad, H., M. Doner, and B. de Meester, "Deformation and Fracture," in *Titanium Science and Technology*, R. I. Jaffee and H. M. Burte, Eds., Plenum Press, New York, pp. 969-1005, 1973.

14. Boyer, R., G. Welsch, and E. W. Collings, *Materials Properties Handbook: Titanium Alloys*, ASM International, Materials Park, OH, 1994.

15. M.A. Myers, Dynamc Behavior of Materials, John Wiley & Sons, Inc., New York, 1994.

16. P.S. Follansbee and C. Frantz, "Wave Propagation in the Split Hopkinson Pressure Bar," Journal of Engineering Materials Technology, 105, pp. 61-66, 1983.

17. P. W. United Technologies, "Quarterly Progress Report," FR24864-4, Subcontract B340842, 1998.

18. Wulf, G. L., "High-Strain Rate Compression of Titanium and Some Titanium Alloys," *International Journal of Mechanical Sciences*, Vol. 21, 713-718, 1979.

19. Follansbee, P. S. and I. G.T. Gray, “An Analysis of the Low Temperature, Low- and High-Strain Rate Deformation of Ti-6Al-4V,” *Metallurgical Transactions* , Vol. 20A, pp. 863-874, 1989.

20. Meyer, L. W., “Strength and Ductility of a Titanium-Alloy Ti-6Al-4V in Tensile and Compressive Loading Under Low, Medium and High Rates of Strain,” in *Titanium Science and Technology*, G. Lutjering, U. Zwicker, and W. Bunk, Eds.: Deutsche Gessellschaft fur Metallkunde, pp. 1851-1858, 1984.

21. Lee, W. S. and C. F. Lin, “Adiabatic Shear Fracture of Titanium Alloy Subjected to High Strain and High Temperature Loadings,” *Journal de Physique IV*, C3, pp. 855-860, 1997.

22. Johnson, G. R., “Strength and Fracture Characteristics of a Titanium Alloy (.06Al, .04V) Subjected to Various Strains, Strain Rates, Temperatures and Pressures,” Naval Surface Weapons Center NSWC TR 86-144, 1985.

23. Johnson, G. R. and T. J. Holmquist, “Test Data and Computational Strength and Fracture Model Constants for 23 Materials Subjected to Large Strains, High-Strain Rates, and High Temperatures,” Los Alamos National Laboratory, LA-11463-MS, 1989.

24. Meyers, M. A., *Dynamic Behavior of Materials*, John Wiley & Sons, Inc., New York, 1994.

25. Follansbee, P. S., “High-Strain-Rate Deformation of FCC Metals and Alloys,” in *Metallurgical Applications of Shock-Wave and High-Strain-Rate Phenomena*, L. E. Murr, K. P. Staudhammer, and M. A. Meyers, Eds, Marcel Dekker, Inc., New York, pp. 451-479, 1986.

26. Frost, H. J. and M. F. Ashby, *Deformation Mechanism Maps*, Pergamon Press, Oxford 1982.

27. Lowden, M. A. W. and W. B. Hutchinson, “Texture Strengthening and Strength Differential in Titanium-6Al-4V,” *Metallurgical Transactions*, Vol. 6A, pp. 441-448, 1975.

28. Chait, R., “The Strength Differential of Steel and Ti Alloys as Influenced by Test Temperature and Microstructure,” *Scripta Metallurgica*, Vol. 7, pp. 351-354, 1973.

29. O’Donnell, R. G. and R. L. Woodward, “Instability During High-Strain Rate Compression of 2024-T351 Aluminum,” *Journal of Materials Science*, Vol. 23, pp. 3578-3587, 1988.

30. Semiatin, S. L. and G.D. Lahoti, “Deformation and Unstable Flow in Hot Torsion of Ti-6Al-4Zr-2Mo-0.1Si,” Metallurgical Transactions, Vol. 12A, pp. 1719-1728, 1981.

31. Semiatin, S. L., G.D. Lahoti, and S. I. Oh, "The Occurrence of Shear Bands in Metalworking," in *Material Behavior Under High Stress and Ultrahigh Loading Rates, 29th Sagamore Army Materials Research Conference Proceedings*, Vol. 29, J. Mescall and V. Weiss, Eds., Plenum Press, New York, pp. 119-159, 1982.

32. Lindholm, U. S. and G. R. Johnson, "Strain-Rate Effects in Metals at Large Shear Strains," in *Material Behavior Under High Stress and Ultrahigh Loading Rates, 29th Sagamore Army Materials Research Conference Proceedings*, Vol. 29, J. Mescall and V. Weiss, Eds., Plenum Press, New York, pp. 61-79, 1982.

33. Brown, W. F. and H. Mindlin, "Aerospace Structural Metals Handbook, Volume 3," CINDAS/USAF CRDA Handbook Operation, pp. 1-17, 1997.

34. ASM International, *Source Book on Industrial Alloy and Engineering Data*, ASM International, Metals Park, OH, 1978.

35. Davis, J. R. et al., *ASM Handbook, Volume 2, Properties and Selection: Nonferrous Alloys and Special-Purpose Materials*, ASM International, Metals Park, OH, 1990.

36. Air Force Materials Laboratory, *Titanium Alloys Handbook*: Metals and Ceramics Information Center, 1972.

37. Brown, W. F., H. Mindlin, and C. Y. Ho, "Aerospace Structural Metals Handbook, Volume 4," CINDAS/USAF CRDA Handbook Operation, 1997.

38. ASM International, "Properties and Selection: Nonferrous Alloys and Special-Purpose Materials," in *ASM Handbook*, Vol. 2, Materials Park, Ohio: ASM International, p. 638, 1990.

39. Lesuer, D. R., G. Kay, and M. LeBlanc, "Modeling Large Strain, High Rate Deformation in Metals," in *Engineering Research, Development and Technology*, Lawrence Livermore National Laboratory, UCRL-53868-98, 1999.

APPENDIX A—PROCEDURES FOR OBTAINING PARAMETERS FOR JOHNSON-COOK MATERIAL MODEL

The parameters in the JC material model are sensitive to the computational algorithm used to calculate these parameters. In this appendix are the procedures used to obtain the constants for equation A-1. The procedures are illustrated for data analysis of the Ti-6Al-4V alloy. For this study, the response at high-strain rate was emphasized. At 25°C and constant strain rate, equation A-11 can be written as

$$\sigma = [A + B\varepsilon^n]C^* \tag{A-1}$$

where C* is a constant. An average stress-strain curve at $\dot{\varepsilon} = 5000\ s^{-1}$ was constructed from the current tension and compression data. The stress at zero plastic strain (AC*) was obtained from the current data and found to be 1230 MPa. The quantity σ-1230 was calculated and plotted versus plastic strain on a log-log plot as shown in figure A-1. The quantities BC* and n were obtained from a least squares fit of the data to a power law equation as BC* = 1220 and n = 0.93. The resulting equation is shown in figure A-1. The agreement between the data (open circles) and the predictions (solid line) is excellent, illustrating that the strain hardening response of the alloy can be represented well by a power law equation.

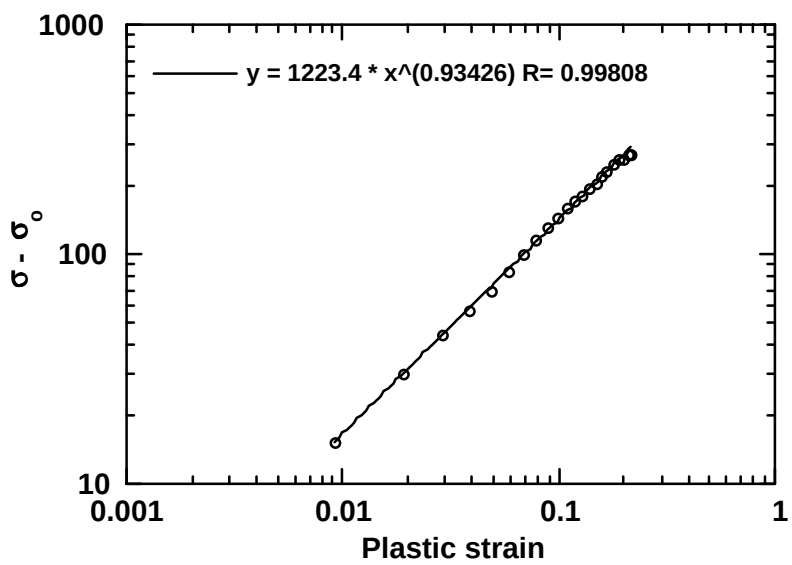

FIGURE A-1. σ-σ_O VERSUS PLASTIC STRAIN FOR THE Ti-6Al-4V ALLOY AT A STRAIN RATE OF 5000 S^{-1}

NOTE: σ_o is the stress at 0 plastic strain.

The parameter C was obtained from σ-$\dot{\varepsilon}$ data. At 25°C and a constant strain, equation A-1 can be written as

$$\frac{\sigma}{\sigma_a} - 1 = C \ln\dot{\varepsilon} \tag{A-2}$$

where σ_a is the stress at $\dot{\varepsilon} = 1\ s^{-1}$. From the data in figure A-1; $\varepsilon = 0.04$, $\sigma_a = 1146$ MPa, and σ_a - 1 is plotted versus $\dot{\varepsilon}$ on a semi-log plot (figure A-2). A least squares fit to the data shows that C = 0.014. The parameters A and B can now be calculated as A = 862 MPa and B = 331 MPa.

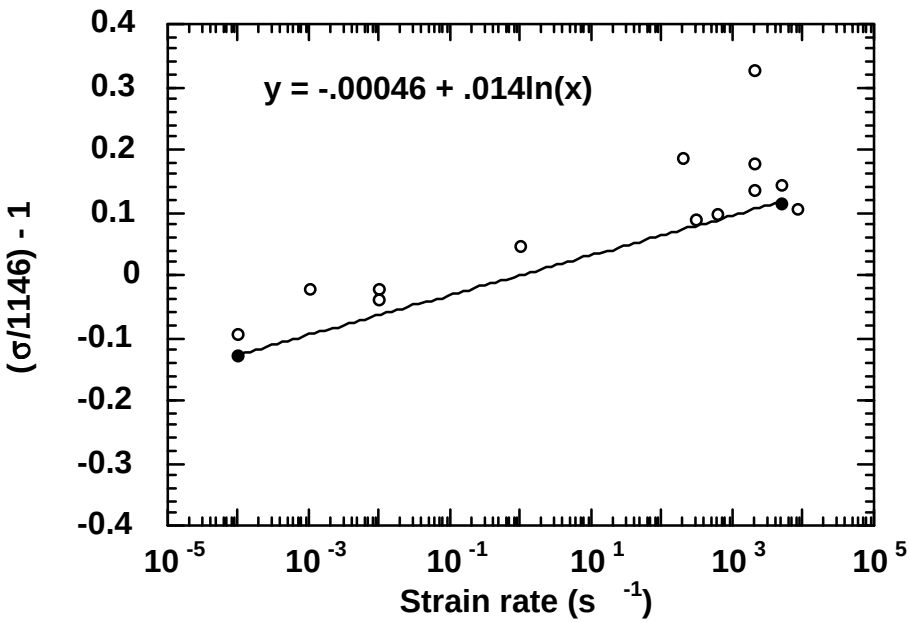

FIGURE A-2. σ/σ_1 VERSUS STRAIN RATE FOR THE Ti-6Al-4V ALLOY

NOTE: σ_1 is the stress at a strain rate of 1 s^{-1}.

The parameter m was determined from the stress-temperature response of the alloy. Data compiled from the literature is presented in figure A-3 and show the stress-temperature response at low and high strain rates and for the high rate data 3 different strains. At constant strain and strain rate, equation A-1 can be written as

$$\frac{\sigma}{\sigma_b} = 1 - T^{*m} \tag{A-3}$$

where σ_b is the stress at 25°C. The data at 2500 s^{-1} and $\varepsilon = 0.04$ were used and σ_b was found to be 1350 MPa. The data was plotted as σ / 1350 versus T*, and the value of m providing the best fit to equation A-3 was established as shown in figure A-4.

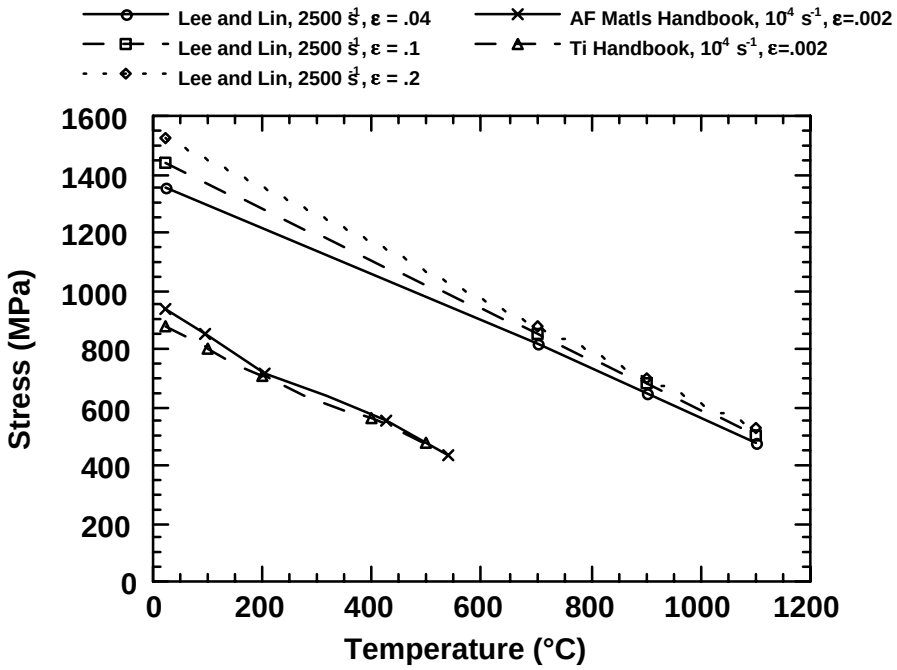

FIGURE A-3. STRESS VERSUS TEMPERATURE FOR THE Ti-6Al-4V ALLOY AT BOTH HIGH-STRAIN RATES AND LOW-STRAIN RATES

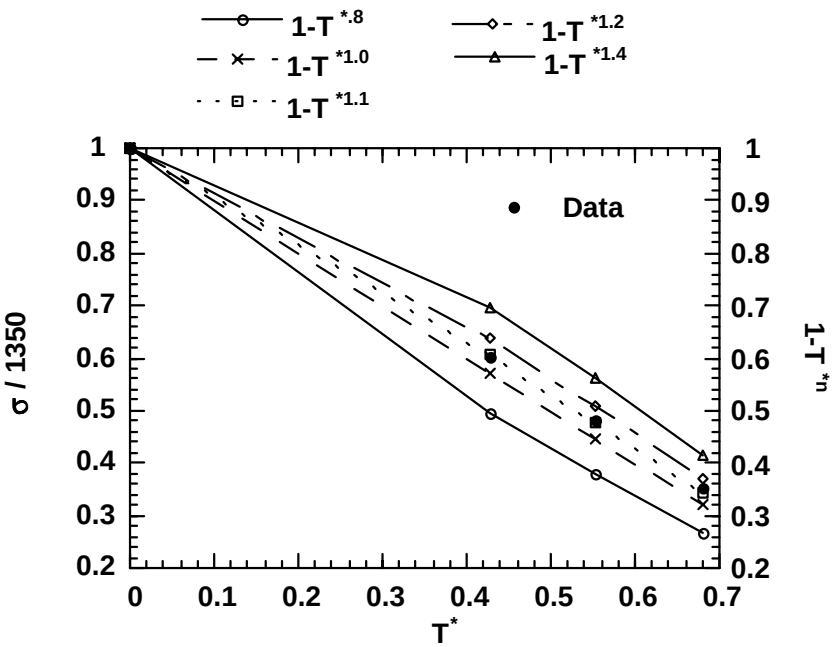

FIGURE A-4. σ/σ_a VERSUS T* FOR THE Ti-6Al-4V ALLOY

NOTE: σ_a is the stress at 298K and T* is defined in the text.